Unsteady Force and Flow Features of Single and Tandem Wheels

Stefano Spagnolo*, Xin Zhang†, Zhiwei Hu‡, Oksana Stalnov§, and David Angland‡
Faculty of Engineering and the Environment, University of Southampton, Southampton, SO16 7QF, UK

Wind-tunnel experiments are presented in this paper for two different models, single wheel and tandem wheels. The tests are performed in the 2.1 m × 1.5 m wind tunnel at the University of Southampton. The aims of the experiment are to gain a better understanding of the flow past simple landing-gear components and to generate a CFD validation database. Since the model is designed to study basic landing-gear components, the wheel geometry is simplified, with no detailed elements in the assembly. The tandem-wheel configuration is formed of two in-line wheels that can be tested at different inter-axis distances and various angles of attack. Mean and unsteady data of aerodynamic loads and on-surface pressures are measured. A vibration test is performed *in situ* on the model assembly to validate the unsteady-load measurements. Particle Image Velocimetry (PIV) is used to acquire the velocity fields in the wake downstream of the model. The results highlight the low sensitivity of the measured quantities to the three versions of the wheel hub on the single wheel. The mean drag coefficients of the tandem wheels show a low sensitivity to the inter-axis distance, which has stronger effects on the mean lift coefficients and the unsteady aerodynamic loads. The angle of attack determines relevant changes in both mean and unsteady quantities. The pressures on the wheel surface are used for gaining a better understanding of the flow regimes and the effect of tripping the flow. Additionally, the PIV data are used to compare the velocity profiles in the wake and identify the wake vortical structures.

Nomenclature

C_D	Drag coefficient (x-axis), $C_D = F_x/(\rho S U_\infty^2/2)$
$\overline{C}_D$	Mean drag coefficient
$C_{D,\mathrm{RMS}}$	Drag coefficient RMS
C_L	Lift coefficient (y-axis), $C_D = F_y/(\rho S U_\infty^2/2)$
$\overline{C}_L$	Mean lift coefficient
$C_{L,\mathrm{RMS}}$	Lift coefficient RMS
C_p	Pressure coefficient $C_p = (p - p_\infty)/(\rho U_\infty^2/2)$
$\overline{C}_p$	Mean pressure coefficient
$C_{p,\mathrm{RMS}}$	Pressure coefficient RMS
D_w	Wheel diameter, m
$\mathbf{F}$	Force, N
k	Turbulent kinetic energy (2D): $k = (\overline{(u'_x)^2} + \overline{(u'_y)^2})/2$, $\mathrm{m}^2/\mathrm{s}^2$
L_w	Inter-axis distance, m
p	Pressure, Pa
p_∞	Free-stream static pressure, Pa
R	Wheel-shoulder radius, m
Re_D	Reynolds number
S	Frontal projected wheel area $S = 0.012\,85\,\mathrm{m}^2$

*PhD student, Airbus Noise Technology Centre, AIAA Student Member
†Airbus Professor of Aircraft Engineering, Airbus Noise Technology Centre, AIAA Associate Fellow, xzhang@soton.ac.uk
‡Lecturer, Airbus Noise Technology Centre, AIAA Member
§Research Fellow, Airbus Aircraft Noise Technology Centre, AIAA Member

T_{xy}	Transfer function
$\mathbf{U}$	Velocity, m/s
$\overline{\mathbf{U}}$	Mean velocity, m/s
U_∞	Free-stream velocity magnitude, m/s
$\mathbf{U}_{\mathrm{RMS}}$	Velocity RMS, m/s
$\mathbf{u}'$	Velocity fluctuation, m/s
x, y, z	Global coordinate system, m
x_p, y_p, z_p	Coordinate system for PIV measurements, m
z_c	Confidence coefficient

Subscripts

f	Relative to front wheel
i	Relative to i-th component
r	Relative to rear wheel
t	Relative to both wheels

Symbols

α	Angle of attack, deg
ϵ_μ	Relative error on the mean
ϵ_σ	Relative error on the standard deviation
ν	Kinematic viscosity of air, m^2/s
ρ	Density of air, kg/m^3
θ	Wheel azimuthal angle, deg

I. Introduction

Most of the literature on the flow past landing gears focuses on aeroacoustics because of the increasingly stringent noise requirements and due to the fact that landing gears are still one of the main sources of noise on civil aircraft [1]. Obtaining a good understanding of the unsteady flow features is not only useful in order to predict noise, but also to correctly estimate the mean and unsteady aerodynamic forces. Venkatakrishnan et al. [2] measured the flow around a rudimentary four-wheel landing gear. It was found that the struts strongly affect the flow field around the two in-line wheels. Mean lift, drag and side forces were provided. Lazos [3] measured the flow velocity in a streamwise plane surrounding the wheels of a four-wheel undercarriage by particle image velocimetry (PIV). The measurement identified different flow states at low frequency. Stalnov et al. [4] experimentally studied a simplified quarter-scale model of a main landing gear. In addition to aeroacoustics measurements, mean aerodynamic loads were measured sequentially on sub-assemblies of the landing gear: from an isolated main strut to a full assembly (main strut, bogie and four wheels), mounting the components one at a time. In this way it was possible to analyze the effect of the various components on the landing-gear aerodynamic loads and noise, but it was not possible to exclude interactions between wheels and struts. The model was studied for horizontal (inclination angle $\alpha = 0\,\mathrm{deg}$), toe-up ($\alpha = 40\,\mathrm{deg}$) and toe-down ($\alpha = -20\,\mathrm{deg}$) bogie configurations. There are other works on aircraft undercarriages, such as the works on the Boeing 777 main landing gear (Humphreys and Brooks [5]), on the Gulfstream G550 nose landing gear (Zawodny et al. [6]), and on the Airbus LAGOON nose landing gear (Manoha et al. [7]). However, unsteady aerodynamic loads were not quantified.

In contrast to the studies described above, in which complex assemblies are considered, there are a number of studies on elementary geometries, representing parts of a landing gear. These studies are generally meant to provide a better understanding of the flow features. For instance the work by Khorrami et al. [8] provided experimental data on tandem cylinders [9]. On the same tandem-cylinders geometry, Xiao and Luo [10] tested the Improved Delayed Detached simulations (IDDES) by Shur et al. [11]. In addition, examples of numerical simulations on the NASA tandem-cylinder benchmark case can be found in the summary by Lockard [12].

Zdravkovich et al. [13] experimentally studied the flow past small aspect ratio cylinders with two free ends in the critical regime $2 \times 10^5 < Re < 6 \times 10^5$. The wake is dominated by a vortex system, that is formed by four vortex filaments. Similar features were noticed on more realistic wheel shapes too. McManus and Zhang [14] performed simulations on the flow past an isolated wheel in contact with the ground, with both fixed and moving ground at a Reynolds number of 5.3×10^6. When the wheel is stationary on the ground, two opposite vortices form on the top wheel shoulders. On the contrary, when the wheel is rotating, the

separated flow on the top part of the wheel forms an arch vortex layer. Later, Zhang et al.[15] experimentally studied the flow past the 33%-scale CADWIE isolated wheel with two different hubs that did not have any significant effect on the flow.

For the purpose of measuring the loads (both mean and unsteady), the strain-gauge based balances are commonly used[16]. The strain is measured on the sensor structure and, after calibration, the forces are estimated. For example, unsteady data for wind aerodynamic loads on wind-turbine models were obtained with a strain-gauge based balance by Hu et al.[17], where the balance was able to capture the unsteady loads at the blade rotation speed and at the higher harmonic frequencies up to three times the rotation speed. In the literature, attempts with direct application of strain gauges in some relevant point of the models exist. For example, Schuster and Byrd[18] applied strain gauges but only the data from the pressure sensors were considered reliable due to the influence of the structural dynamic modes on the strain gauges. For short-duration force measurements (e.g., Robinson and Hannemann[19]), models and special calibration rigs have to be prepared. This is more complex than the previous case because the model is designed for the purpose of the dynamic calibration.

Another approach is the use of pressure sensitive paint to obtain the loads by integrating the measured surface pressure[20] and piezoelectric sensors for high frequency local information for both surface shear stress and surface pressure[21,22,23]. In some specific cases, more complex techniques can be applied. For example, on two-dimensional geometries, time-resolved PIV can be used to estimate the forces on the model[24], whilst small-size models can be supported by a magnetic suspension system[25].

The current work aims to achieve a better understanding of mean and unsteady characteristics of the flow around landing-gear bogies, which can be used later in the project to improve the efficiency and accuracy of landing-gear aerodynamic loads CFD prediction. Loads, surface pressures, and velocity fields are measured on a new geometry that represents a simplified model of a landing gear: wheels in single and tandem configurations. The tandem configuration represents half of a four-wheel bogie without any interference from struts, doors, bogie beams, axles, etc. A preliminary vibration test[26] is used to assess the capability of the balance to measure unsteady loads. As a separate part of the same project (not discussed in this paper), advanced simulation techniques will be developed around the current experimental geometry to achieve more accurate and efficient predictions for the flow past landing gears.

II. Experimental Setup and Procedures

A. Test facility and model geometry

The experiments were conducted at the University of Southampton. The facility is a closed-circuit closed-test-section wind tunnel with a cross-section of 2.1 m×1.5 m. The wind tunnel can run at free-stream velocities U_∞ between 10 m/s and 48 m/s corresponding to a Reynolds number $Re_D = U_\infty D_w/\nu$ range between 1.2×10^5 and 5.8×10^5 for the current model, where D_w is the wheel diameter and ν is the kinematic viscosity of air.

The current model consists of two wheels in tandem. The wheel is a generic model of a landing-gear wheel, as shown in Figure 1(a). The geometric parameters are defined as follows: the wheel diameter D_w is 0.181 m, the width W is $0.4D_w$ and the fillet radius R is $0.1D_w$ (uniform). Measurements are performed in different configurations for three inter-axis distances L_w ($1.1D_w$, $1.3D_w$ and $1.5D_w$) and two angles of attack α (0 deg and 20 deg). The wheels are supported by streamlined struts to minimize the interference. A picture of the wind-tunnel assembly can be found in Figure 1(b). The two supports are tapered zero-sweep half wings with a NACA-0024 cross section. The support length is 300 mm and the taper ratio (tip/root chord ratio) is 0.46. The supports are mounted to have, for all the tested configurations, zero angle of attack. The blockage ratio is between 0.5% and 1%, depending on the specific configuration.

During the force measurements, several tripping devices were applied on the wheel surface, including those made of zig-zag tapes and roughness strips made of number 60 grit, in a range of tripping sizes and locations. This study mainly tests the wheel with a flat hub cover, but two additional hubs were manufactured and tested on the single-wheel configuration. The first modified cover has an axisymmetric convex cavity, whilst the second modified cover has the same convex cavity plus a concentric axisymmetric protrusion representing a simplified hub. The schematic cross-sections for the three covers are presented in Figure 2.

The model is manufactured by means of rapid prototyping techniques. In detail, the wheels are made by 3D printing with a LS600 photopolymer machine, while the supports are made of carbon-fibre reinforced plastic (CFRP) and aluminium alloy. The interfaces with the wind-tunnel frame are standard aluminium profiles plus a machined aluminium plate. The manufacturing tolerances for the external wheel surface can

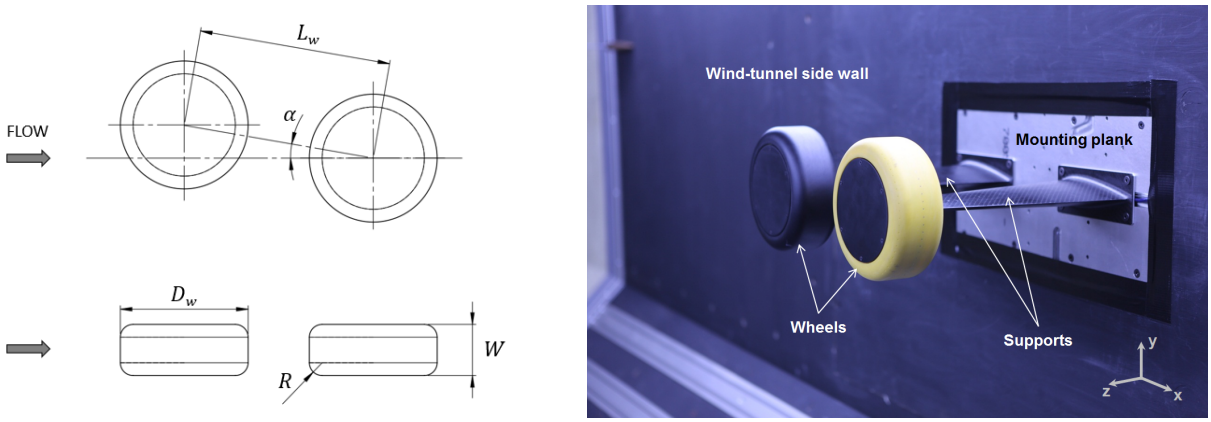

(a) Schematic drawing of a generic tandem-wheel configuration.

(b) Picture of the wind-tunnel model assembly.

Figure 1. Tandem-wheels experimental assembly with the main geometric parameters and the global reference system (x the streamwise, y the vertical, and z the spanwise direction).

be estimated to be ± 0.1 mm with respect to the axis system of the 3D-printing machine. The maximum error on the wheels position is ± 1 mm.

B. Loads and pressure acquisition systems

The current experiments measure the forces acting on the two wheels separately, to characterize the loads in terms of both mean and unsteady values (i.e., the root mean square of the force signal).

Since the existing wind-tunnel balance is not sensitive enough for the expected order of magnitude of the forces to be measured, an ATI mini40 sensor (a 6-axis strain-gauge based transducer) is mounted inside the wheels. Thus the sensor measures only the loads acting on the wheels external surface. All the results in this paper are obtained in acquisition intervals shorter than 240 seconds, in which the maximum observed drift of the forces is 0.02 N. A repeatability test was done as part of the experiment and confirmed that the relative errors on the mean force coefficients are within 1% at a speed of 40 m/s.

An additional wheel with identical external shape is manufactured for on-surface data collection. This additional model is designed to host a miniature pressure scanner with multiple channels (instead of the balance) inside the wheel. The pressure scanner is the miniature 64-channels Scanivalve ZOC33. The pressures were acquired with an in-house dSpace system. The model is manufactured with 21 equally-spaced holes for pressure taps along a 120-deg sector along the center-line circumference. Rotating the wheel four times (90 deg rotation each) allows for acquiring the full circumferential pressure data with a 30 deg overlap for each rotating position. Overall, surface pressure data are available for 60 points equally spaced in the azimuthal angle θ, as defined in Figure 3, on the full center-line circumference.

C. Particle Image Velocimetry (PIV) setup

Particle Image Velocimetry (PIV) can capture instantaneous flow fields. The technique consists of acquiring two consecutive pictures and estimating the displacement of the particles in the flow between the two subsequent pictures. The current PIV setup uses a single 4 Megapixel camera to acquire the two in-plane components of a square frame behind the rear wheel. The reference axes x_p-y_p for the PIV frames are positioned at the most downwind point of the rear wheel, as illustrated in Figure 4. For single-wheel configurations the front wheel is removed. The fields are measured on the Slice A (wheel center-line, $z = 0$) and on the Slice B (inner shoulder, $z = -W/2$), both shown in Figure 4.

To capture a 250 mm $\times$ 250 mm frame (in Figure 4) at a distance of approximately 1.8 m from the target plane, a 105-mm Sigma lens is mounted on the camera, outside the wind tunnel. The laser, a Quantel Twins BSL 200, is configured to fire two consecutive shots with a 20 μs delay. The frame acquisition is repeated at a frequency of 3.63 Hz for 500 frames. The results reported in Section III are shown for a frame of 200 mm $\times$ 200 mm, after removing the part close to the model, where errors exist due to reflections.

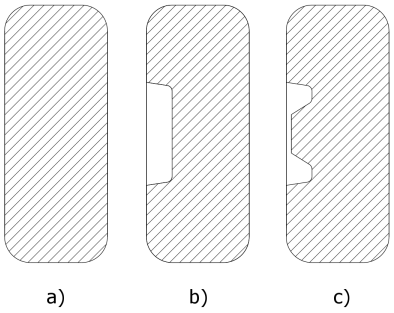

Figure 2. Wheel frontal cross-section for the three different covers: a) flat cover; b) cavity only; c) cavity with hub.

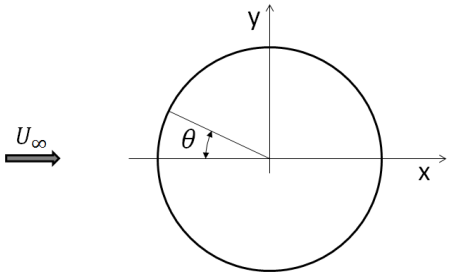

Figure 3. Pressure taps reference system. For tandem-wheels configuration, for each wheel, the zero θ is at the most windward point.

To estimate the maximum relative errors, ϵ_μ and ϵ_σ, on the resulting mean velocity component $\overline{U}_i$ and its standard deviation $U_{\mathrm{RMS},i}$, the following formulas (Grant and Owens [27]) are applied:

$$\epsilon_\mu = \frac{z_c U_{\mathrm{RMS},i}}{\overline{U}_i \sqrt{N}} \tag{1}$$

$$\epsilon_\sigma = \frac{z_c}{\sqrt{2N}} \tag{2}$$

where N is the number of samples and z_c is the confidence coefficient (here assumed equal to 1.96 for a 95% confidence level).

For the current tests, the error on the mean fields is lower than 1.6 m/s and the error on the standard deviation is within 1 m/s (both with a confidence level of 95%). The errors are higher in the region close to the wheel, and become smaller further away. This is because the turbulence level is high affecting the statistical error estimation of Equation (1) and Equation (2), and the reflections cause more loss of valid vectors due to the lower signal-to-noise ratio.

D. Vibration test

The strain-gauge based balance inside the wheel model quantifies the forces by means of the strain of the balance itself. For dynamic load measurements, at high frequencies the sensor measures the dynamic response of the model assembly [26]. In addition, the dynamic response is generally different in each direction, and the modes are coupled: this means that even forcing the model in one direction only, the balance can measure non-zero dynamic values in the other components. Here, the aerodynamic unsteady loads are validated by a preliminary vibration test to identify the model dynamic response. The vibration test must be performed *in situ*: the model is mounted in the wind tunnel and an electro-magnetic shaker is used to force the model in different spots, along different directions.

The vibration-test equipment consists of a Data Physics Signal-Force GW-V4/PA30E shaker and a Dytran 1053V piezoelectric force sensor. The shaker can provide both a random and a sinusoidal force, which is transmitted to the model through the piezoelectric force sensor. Thus, the force measured by the mini40 sensor and the excitation force are simultaneously acquired. To understand the accuracy of the measured dynamic values, the transfer function between the external forces and the measured values from the balance can be calculated. The results of the procedure for the forces in the two axes x and y are illustrated in Figure 5, which shows that the unsteady load data measured by the balance are consistent with the externally applied loads up to approximately 30 Hz. The transverse sensitivity can be associated with modes coupling phenomena, positioning or alignment errors in the shaking system, and additional modes relative to the wind tunnel mountings or to minor features of the model. The transverse sensitivity (not shown in the plot) is within 15% of the external load. Due to the high complexity of the model and its position in the wind tunnel, both with the finite elements simulations and the vibration test, it is hard to clearly identify the reasons of the considered phenomenon. The transfer functions of the moments show analogous results, with less accuracy, due to the lower intensity of the moments applied. In the following sections of the current work, only the F_x and F_y forces are considered, both in terms of mean loads and unsteady loads.

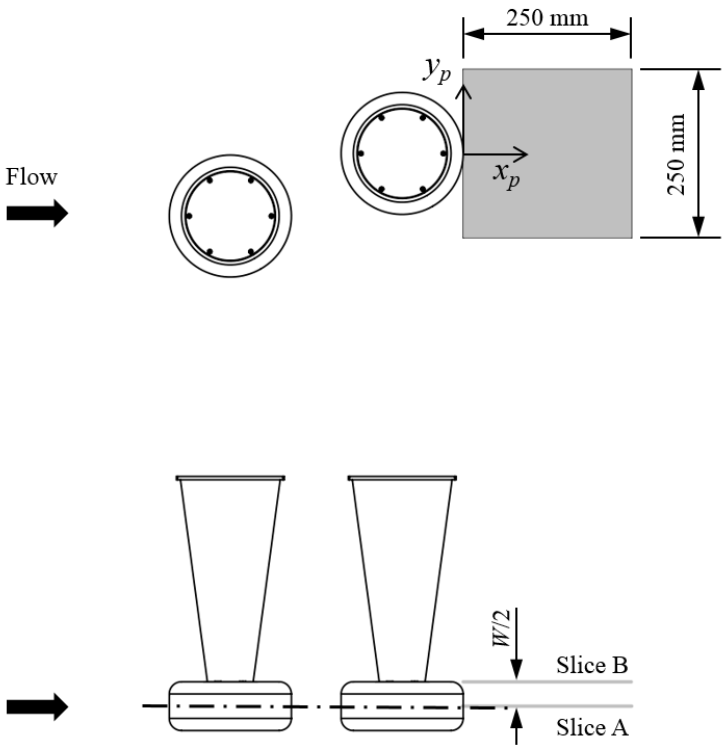

Figure 4. Scheme of the PIV original target slice (in grey) and the PIV reference system (x_p, y_p). The sizes are expressed in millimeters.

III. Results

A. Force Measurements

1. Mean loads

The mean drag coefficient $\overline{C}_D$ of the single-wheel and tandem-wheel reference configurations (with $L_w = 1.5D_w$ and $\alpha = 0\,\text{deg}$) are shown in Figure 6 as functions of the Reynolds number Re_D. The wheel cover used in this test is the flat cover, i.e. configuration *a* in Figure 2. At the free-stream velocity of 40 m/s ($Re_D = 4.8 \times 10^5$), for the single-wheel case $\overline{C}_D$ is 0.229, whilst for the reference tandem-wheel case $\overline{C}_D$ is 0.082 on the front wheel and 0.336 on the rear wheel. For Reynolds numbers in the range $3.6 \times 10^5 < Re_D < 5.7 \times 10^5$, the mean drag coefficient does not show marked variations.

As mentioned in Section II, the single wheel was tested also with two additional versions of the cover (Figure 2). The mean drag coefficient for the single wheel at 40 m/s was 0.238 with the cavity-only cover, while it was 0.241 with the cover including the simplified hub. Generally, the effect of the two additional covers is small, since it implies an increase in drag coefficient within 5% from the baseline geometry with flat cover. This is also confirmed by previous tests on the CADWIE wheel[15]. For this reason, no further test was performed with covers other than the flat baseline geometry.

The Reynolds number for the current model is not representative of a full-scale landing gear in flight conditions, thus the geometry was tested with tripping devices on. The tripping techniques used are the conventional zig-zag tape and the Grit60 roughness strip. The zig-zag tape is applied on the front part of the wheel at $\pm 45\,\text{deg}$ and on the wheel shoulders, the Grit60 tape is applied on the full-shoulders circle plus two horizontal Grit60 stripes at $\pm 60\,\text{deg}$. For the tandem-wheel configuration, the tripping is applied only on the front wheel. The effect of the zig-zag tape on the single wheel is marginal on the drag coefficient, but generates non-zero lift coefficient ($|\overline{C}_L| \ll \overline{C}_D$), whilst the Grit60 generates a 30% drag increase and lift coefficient comparable to the drag coefficient ($\overline{C}_D \approx 0.3$ and $\overline{C}_L \approx 0.2$). There is mean lift in spite of

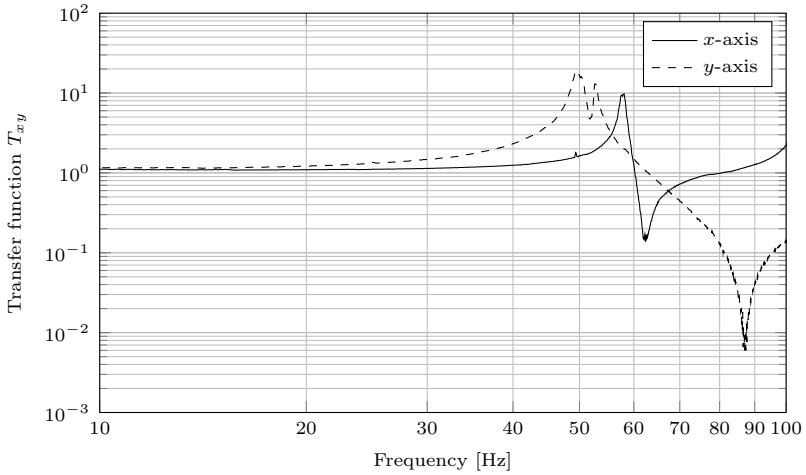

Figure 5. Transfer function from the vibration test with external force applied along the x-axis and along the y-axis.

symmetric geometries and symmetric tripping devices. The randomness of the mean lift sign excludes the effect of positioning errors on the results. On the contrary, the results of the tandem wheels with zig-zag tape show a drag coefficient 30% higher than the untripped case. Since the tripping devices did not show the same repeatability as the baseline (without tripping device), no load data are provided here for the tripped configurations.

The geometric parameters that were analyzed during the experiments are L_w/D_w ratio and α angle of attack. The front-wheel drag coefficient $\overline{C}_{Df}$ and rear-wheel drag coefficient $\overline{C}_{Dr}$ are summarized in Table 1, together with the total drag coefficient $\overline{C}_{Dt}$ from both wheels. The list includes three different L_w/D_w ratios at zero angle of attack ($L_w/D_w = 1.1$, 1.3 and 1.5) and two angles of attack for $L_w/D_w = 1.3$ ($\alpha = 0\,\text{deg}$ and $\alpha = 20\,\text{deg}$).

Table 1. Effect of the geometric parameters on mean loads.

Configuration		$\overline{C}_{Df}$	$\lvert\overline{C}_{Lf}\rvert$	$\overline{C}_{Dr}$	$\lvert\overline{C}_{Lr}\rvert$	$\overline{C}_{Dt}$
$\alpha\,[\text{deg}]$	L_w/D_w					
0	1.1	0.093	0.137	0.305	0.004	0.398
0	1.3	0.060	0.048	0.337	0.003	0.397
0	1.5	0.082	0.002	0.336	0.024	0.418
20	1.3	0.181	0.005	0.384	0.032	0.565

A change in the inter-axis distance has the main effect of redistributing the drag coefficient between the wheels, without dramatically affecting the total drag coefficient (differences within 5%). The most relevant phenomenon to note is the flow asymmetry for small inter-axis distance, which is revealed by the non-zero mean lift coefficients. This is due to either an increased relative error on the zero angle due to the reduced distance between the wheels or to a higher sensitivity of the flow itself to the perturbation. On the contrary, the angle of attack has the effect of increasing the total drag coefficient by 42%. A global drag increase is expected due to the larger projected frontal area, but also the drag distribution on the two wheels is different from the respective $\alpha = 0\,\text{deg}$ case.

The front lift coefficient $\overline{C}_{Lf}$ is not zero in the lowest and in the medium distances ($L_w/D_w = 1.1$ and 1.3) in spite of a zero angle of attack. Similar asymmetric flows were previously observed by Khorrami et al. [8] on tandem cylinders, in similar Reynolds number ranges. On the contrary, with the highest $L_w/D_w = 1.5$ the flow is symmetric, i.e. the mean lift is small for both wheels. Within the tested range, the front lift coefficient decreases with increasing L_w/D_w ratio, whilst the rear lift coefficient increases. But the maximum rear lift coefficient is never as high as the front lift coefficient in the inter-axis distance of $L_w = 1.1D_w$.

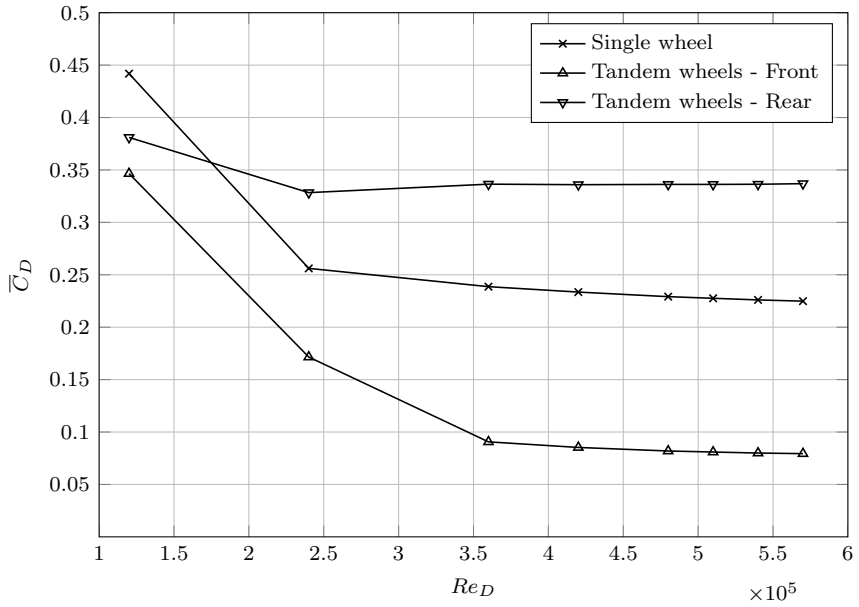

Figure 6. Mean drag coefficient $\overline{C}_D$ as a function of the Reynolds number Re_D for single and tandem wheels, flat cover.

2. Unsteady loads

The unsteady loads were measured up to 1000 Hz, but due to the balance response, only the lowest part of the spectra is independent from the mounting setup. A nominal upper limit of 30 Hz (from Section II) is adopted in this chapter when calculating the standard deviations of the force coefficients. The standard deviations are mainly Reynolds independent in the upper part of the tested Reynolds range.

Concerning the single wheel, the standard deviations are $C_{D,\mathrm{RMS}} = 0.005$ for the drag coefficient and $C_{L,\mathrm{RMS}} = 0.032$ for the lift coefficient. For the tandem-wheel case the standard deviations are given in Table 2. In general, the standard deviations are higher for the tandem-wheel case than for the single-wheel case. The lift coefficient RMS is generally higher than the the respective drag coefficient RMS.

Table 2. Effect of the geometric parameters on loads standard deviations.

Configuration		$C_{Df,\mathrm{RMS}}$	$C_{Lf,\mathrm{RMS}}$	$C_{Dr,\mathrm{RMS}}$	$C_{Lr,\mathrm{RMS}}$
α [deg]	L_w/D_w				
0	1.1	0.021	0.015	0.016	0.025
0	1.3	0.010	0.074	0.016	0.050
0	1.5	0.005	0.036	0.011	0.058
20	1.3	0.013	0.017	0.012	0.031

B. Pressure Measurements

To gain a better understanding of the flow on the wheels, on-surface pressures are measured with pressure taps on the wheel center-line circumference. The circumference angle for each wheel is measured clockwise from the front stagnation point, as shown in Figure 3. In the experiment, the static reference pressure p_∞ and the reference dynamic pressure $\rho U_\infty^2/2$ are directly provided by a Pitot tube positioned in the test section. Two different sampling frequencies were tested, 113.6 Hz and 568.2 Hz for each channel, and no difference was found in the results.

The resulting pressure coefficient C_p for the clean and the tripped configuration on the single wheel are shown in Figure 7. For the tripped case, the values close to the tripping positions are affected by the tripping

device, thus any difference in those parts of the plot must be considered as the result of the test methodology and, for the sake of clarity, the points were removed from the plots. The difference in the mean values in the region of θ between 90 and 120 deg is due to higher turbulence developed in the boundary layer in the tripped case.

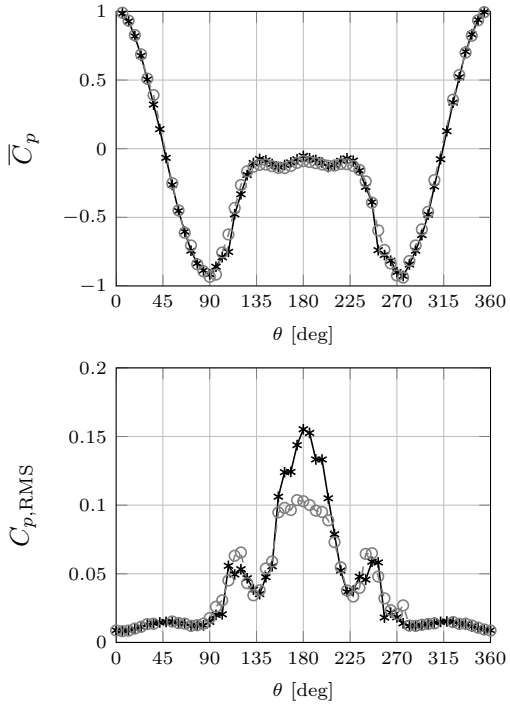

Figure 7. Single wheel: mean and RMS values of the pressure coefficient C_p along the wheel centre line, comparing the untripped (—∗—) and the tripped (- ⊖ -) case.

Results of the tandem-wheel case at two different L_w/D_w ratios are illustrated in Figure 8(a) for the front wheel and in Figure 8(b) for the rear wheel. The tripped configurations are not illustrated. Two symmetric high-pressure areas ($C_p \approx 0.8$) are found at ± 30 deg on the rear wheel. The differences between the two configurations in terms of mean pressure coefficients are minimal, confirming the trend observed in the measured forces. The most significant differences are in the standard deviation of the pressures, especially in the aft part of the front wheel.

C. Flow fields from PIV

With the current PIV setup (described in Section II) two longitudinal slices of the velocity field were acquired in various configurations at constant-z planes. The resulting mean velocity magnitude flow past the single wheel is shown in Figure 9(a). A sample result for one of the tandem-wheel cases ($L_w = 1.5D_w$, $\alpha = 0$ deg) is presented in Figure 9(b).

The wake structures firstly identified by Zdravkovich et al. [13] can be observed from the comparison of the the PIV slices on the wheel center line (Slice A in Figure 10(a)) and the wheel shoulder (Slice B in Figure 10(b)). The y-component of the mean velocity is oriented in opposite directions on the wheel center line and on the wheel shoulder. This highlights the presence of a vortex that is generated on the wheel shoulder.

More interesting is the comparison in Figure 11 between the velocity profiles on the plane at a given streamwise location, one wheel diameter downstream of the rear wheel axle. The asymmetric behavior identified during the load analysis for the low L_w/D_w case can be found also in the velocity data.

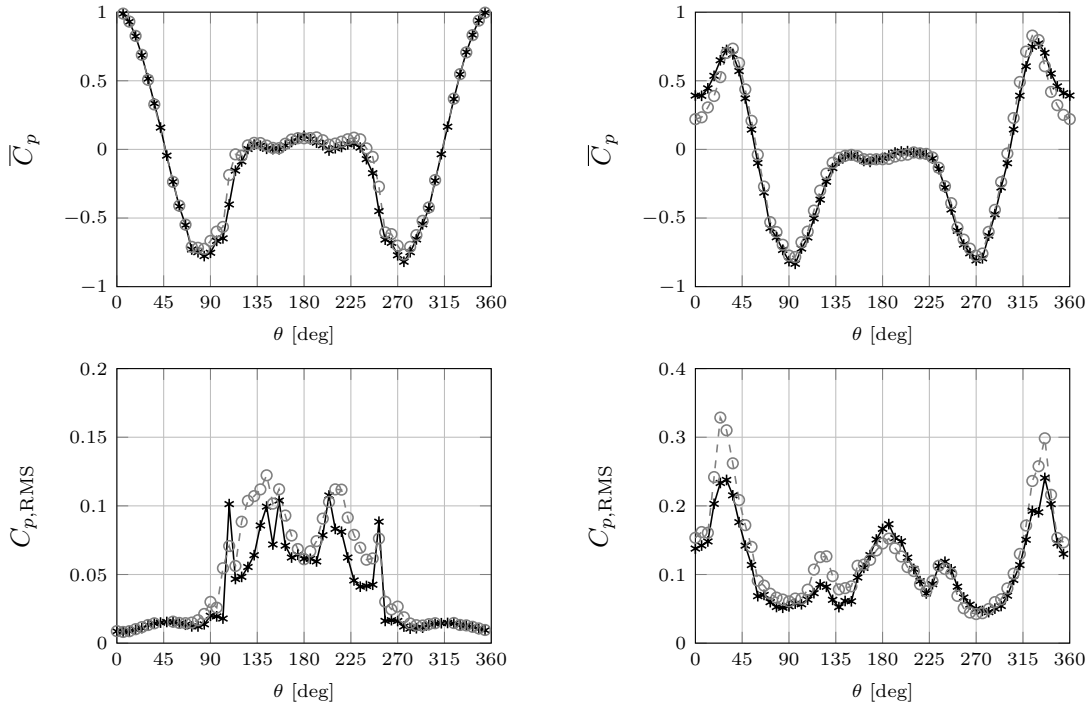

(a) Front wheel (b) Rear wheel

Figure 8. Mean and RMS values of the pressure coefficients C_p along the wheel center line, comparing the tandem wheels configurations $L_w/D_w = 1.3$(- ⊖ -) and $L_w/D_w = 1.5$ (—✶—), both at $\alpha = 0\,\mathrm{deg}$, both untripped.

IV. Conclusions

Aerodynamic loads, pressures and velocity fields were experimentally measured for the flow past single and tandem wheels. The tandem-wheel model represents half of a simplified four-wheel landing gear. The aerodynamic forces were validated with a preliminary vibration test on the model structure, to estimate the dynamic response of the balance. The wind-tunnel tests were performed in the $2.1\,\mathrm{m} \times 1.5\,\mathrm{m}$ wind tunnel at the University of Southampton, and were repeated for the listed configurations (various inter-axis distances and various angles of attack). One of the main findings of this experiment is the limited effect of the inter-axis distance on the global drag coefficient in the tested range of L_w/D_w (inter-axis distance over diameter ratio) between 1.1 and 1.5, while the effect on the standard deviations is more relevant. For this reason, mean and unsteady values should be both analyzed. In spite of zero angle of attack, a non-symmetric mean flow was found for small L_w/D_w ratios. Similar problems of asymmetric flows become relevant also when applying tripping devices. The presence of the hub cavity on the wheel side did not give any relevant change to the force coefficients, confirming the previous findings. The PIV images confirmed the trend observed with the force measurements and allowed the identification of the expected vortical system in the wake from the comparison between the vertical velocities. A transverse slice of the flow field (not measured here) would allow the identification of the exact position of the vortices.

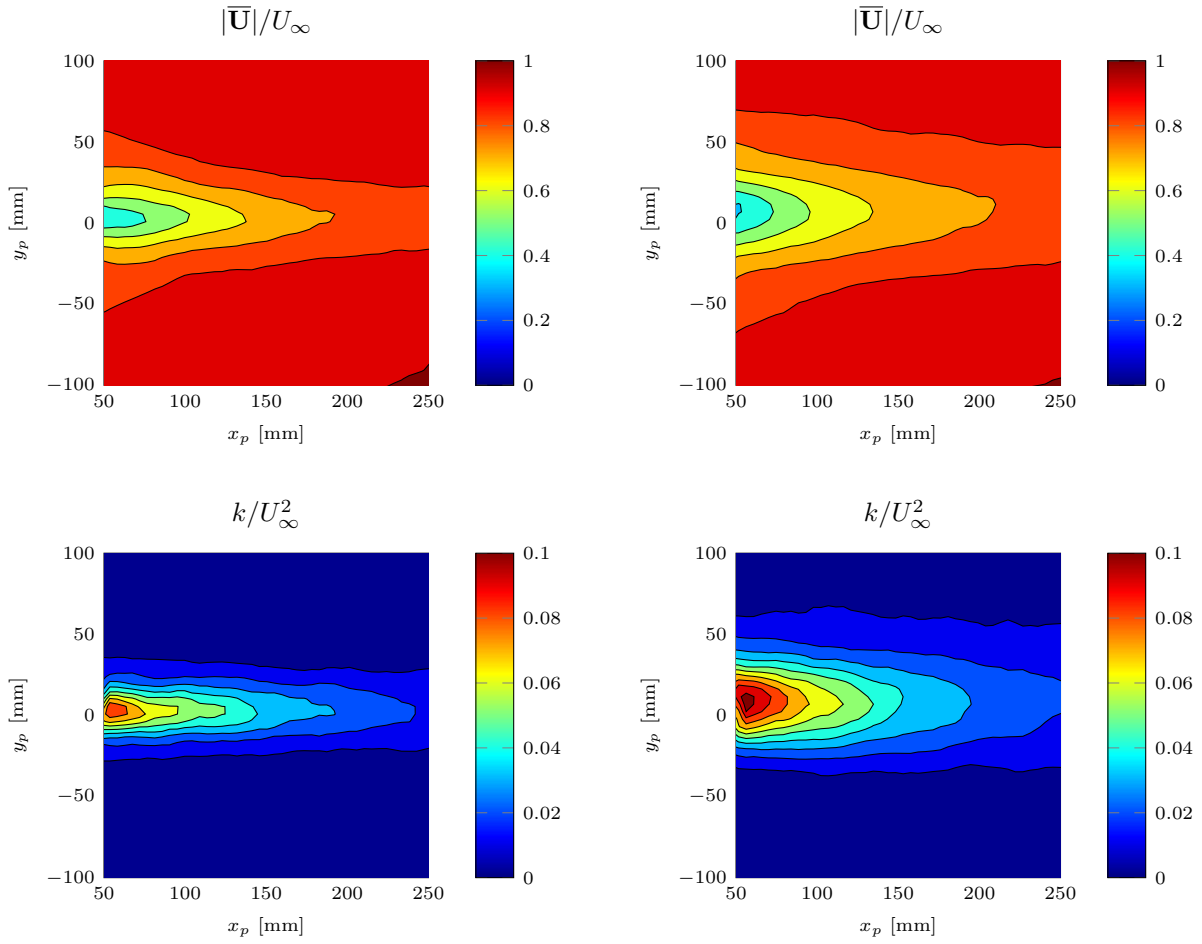

(a) Single wheel

(b) Tandem wheel

Figure 9. Mean velocity magnitude |U| and turbulent kinetic energy k fields in non-dimensional form (Slice A) for single wheel and tandem wheels ($L_w = 1.5D_w$, $\alpha = 0\,\mathrm{deg}$).

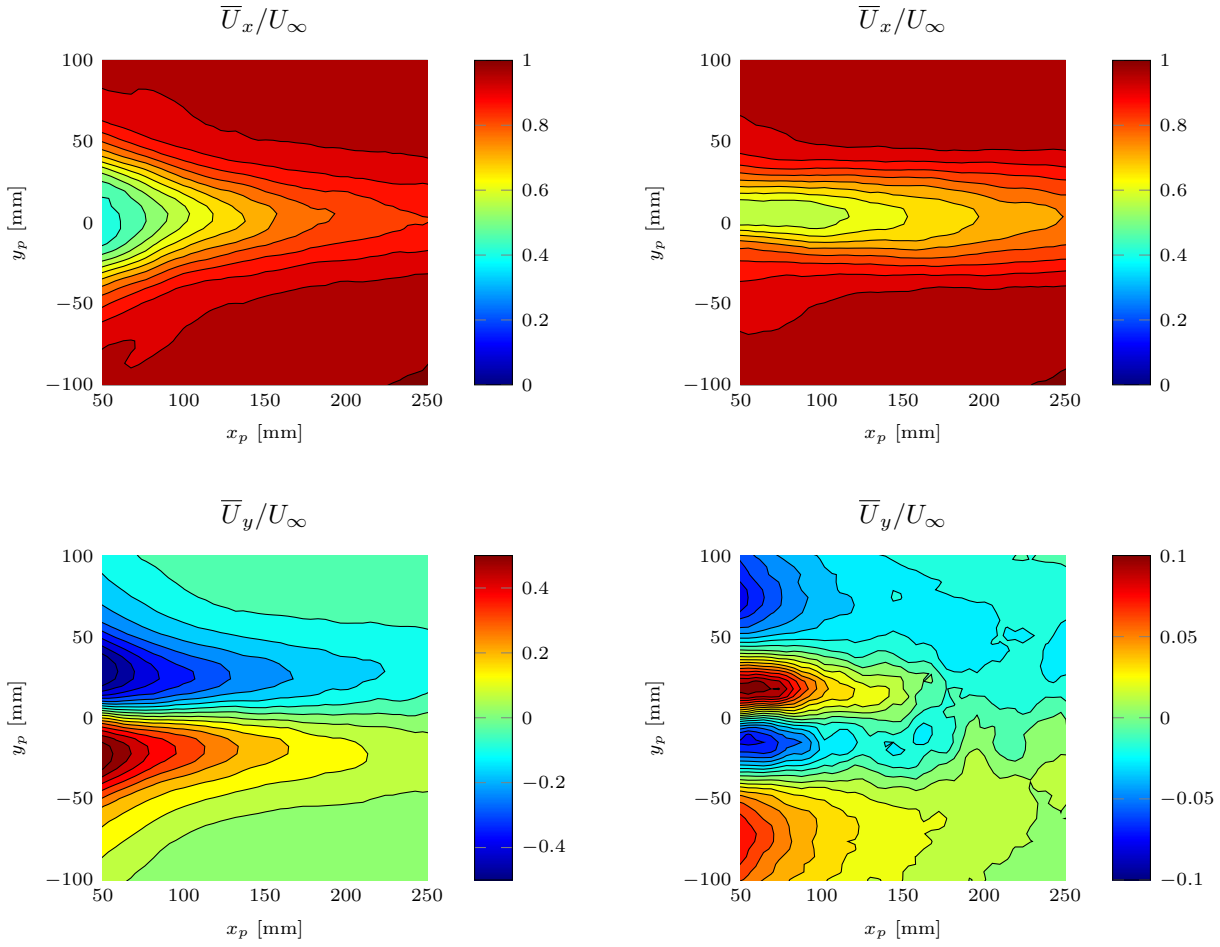

(a) Slice A

(b) Slice B

Figure 10. Mean streamwise velocity $\overline{U}_x$ and mean vertical velocity $\overline{U}_y$ in non-dimensional form for single wheel in the two slices.

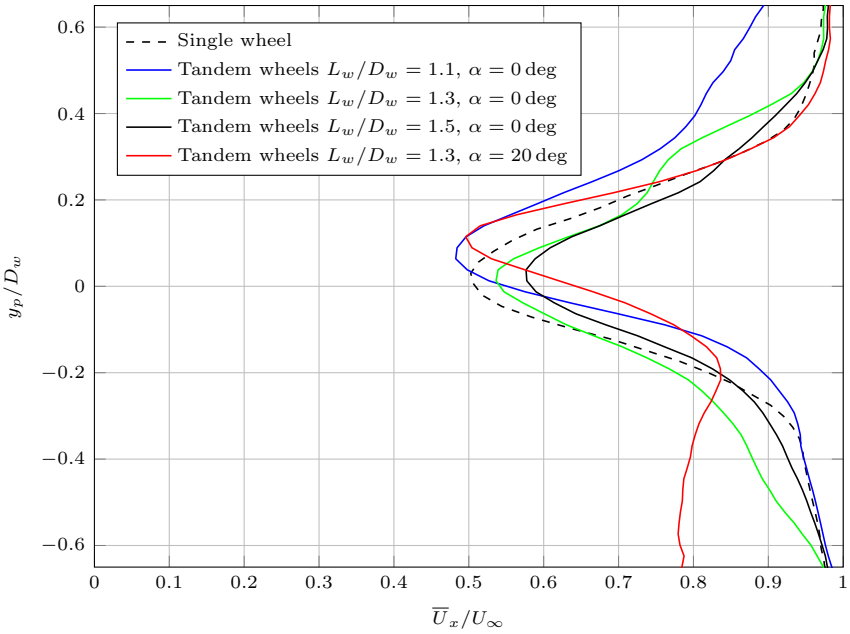

Figure 11. Profiles of non-dimensional mean streamwise velocity $\overline{U}_x$ at distance D_w downstream of the rear wheel axle (Slice A).

Acknowledgments

The funding for this work is provided by the UK Aerospace Technology Institute under the Advanced Landing Gear Aero-Loads and Aero-Noise Prediction (ALGAAP) project. In particular, the authors are thankful to Alan Shepherd (Airbus) for his advice. The wind-tunnel staff at the University of Southampton are kindly acknowledged for their technical support.

References

[1] Dobrzynski, W. Almost 40 years of airframe noise research: what did we achieve? *Journal of Aircraft*, 47(2):353–367, March-April 2010.

[2] Venkatakrishnan, L., Karthikeyan, N., and Mejia, K. Experimental studies on a rudimentary four-wheel landing gear. *AIAA Journal*, 50(11):2435–2447, November 2012.

[3] Lazos, B. S. Mean flow features around the inline wheels of four-wheel landing gear. *AIAA Journal*, 40 (2):193–168, 2002.

[4] Stalnov, O., Windiate, S., Angland, D., Zhang, X., and Ashworth, R. On the contribution of individual components to landing gear loads and noise. AIAA Paper 2013-3153, 2013.

[5] Humphreys, W. M. J. and Brooks, T. F. Noise spectra and directivity for a scale-model landing gear. AIAA Paper 2007-3458, 2007.

[6] Zawodny, N. S., Liu, F., Yardibi, T., Cattafesta, L., Khorrami, M. R., Neuhart, D. H., and Van de Ven, T. A comparative study of a $^1/_4$-scale Gulfstream G550 aircraft nose gear model. AIAA Paper 2009-3153, 2009.

[7] Manoha, E., Bulté, J., and Caruelle, B. Lagoon: An experimental database for the validation of CFD/CAA methods for landing gear noise prediction. AIAA Paper 2008-2816, 2008.

[8] Khorrami, M. R., Choudhari, M. M., Lockard, D., Jenkins, L. N., and McGinley, C. B. Unsteady flowfield around tandem cylinders as prototype component interaction in airframe noise. *AIAA Journal*, 45(8): 1930–1941, 2007.

[9] Sumner, D. Two circular cylinders in cross-flow: A review. *Journal of Fluid and Structures*, 26:849–899, 2010.

[10] Xiao, Z. and Luo, K. Numerical simulations of tandem cylindes with subcritical spacing. AIAA Paper

2013-2209, 2013.

[11] Shur, M. L., Spalart, P. R., Strelets, M. K., and Travin, A. A hybrid RANS-LES model with delayed DES and wall-modeled LES capabilities. *International Journal of Heat and Fluid Flow*, 29:1638–1649, 2008.

[12] Lockard, D. P. Summary of the tandem cylinder solutions from the benchmark problems for airframe noise computations-i workshop. AIAA Paper 2011-353, 2011.

[13] Zdravkovich, M. M., Flaherty, A. J., Pahle, M. G., and Skelhorne, I. A. Some aerodynamic aspects of coin-like cylinders. *J. Fluid Mech.*, 360:73–84, 1998.

[14] McManus, J. and Zhang, X. A computational study of the flow around an isolated wheel in contact with the ground. *Journal of Fluids Engineering*, 128(3):520–530, 2005.

[15] Zhang, X., Ma, Z., Smith, M., Sanderson, M., and Bissessur, P. Aerodynamic and acoustic measurements of a single landing gear wheel. AIAA Paper 2013-2160, 2013.

[16] Tropea, C., Yarin, A. L., and Foss, J. F., editors. *Springer Handbook of Experimental Fluid Mechanics*. Springer, 2003.

[17] Hu, H., Yang, Z., and Sarkar, P. Dynamic wind loads and wake characteristics of a wind turbine model in an atmospheric boundary layer wind. *Experiments in Fluids*, 52:1277–1294, 2012.

[18] Schuster, D. M. and Byrd, J. E. Transonic unsteady aerodynamics of the F/A-18E at conditions promoting abrupt wing stall. AIAA Paper 2003-0593, 2003.

[19] Robinson, M. and Hannemann, K. Short duration force measurements in impulse facilities. AIAA Paper 2006-3439, 2006.

[20] De Lucca, N., Gordeyev, S., Jumper, E., Thordahl, J., and Wittich, D. J. The estimation of the unsteady aerodynamic force applied to a turret in flight. AIAA Paper 2013-3136, 2013.

[21] Nitsche, W. and Mirow, P. Piezo-electric foils as a means of sensing unsteady surface forces. *Experiments in Fluids*, 7:111–118, 1989.

[22] Baban, F., So, R., and Ötügen, M. Unsteady forces on circular cylinders in a cross-flow. *Experiments in Fluids*, 7:293–302, 1989.

[23] Capece, V. and Fleeter, S. The unsteady aerodynamics of a first stage stator vane row. *Experiments in Fluids*, 4:72–78, 1986.

[24] Kurtulus, D., Scarano, F., and David, L. Unsteady aerodynamic forces estimation on square cylinder by TR-PIV. *Experiments in Fluids*, 42:185–196, 2007.

[25] Sawanda, H. and Suda, S. Study on aerodynamic force acting on a sphere with and without boundary layer trips around the critical Reynolds number with a magnetic suspension balance system. *Experiments in Fluids*, 50:271–284, 2011.

[26] Piersol, A. G. and Paez, T. L. *Harris' Shock and vibration handbook*. McGraw-Hill Handbooks, 6th edition, 2010.

[27] Grant, I. and Owens, E. H. Confidence interval estimates in PIV measurements of turbulent flows. *Applied optics*, 29(10):1400–1402, April 1990.